

Check for updates



www.chemsuschem.org

# Modulation of Self-Assembly and Enhanced Photocatalytic H<sub>2</sub> Production by Porphyrin-Dipeptide Conjugates

Evitina Triantafyllou, Emmanouil Nikoloudakis,\* Sotiris Psilodimitrakopoulos, Dimitrios Kavalieros, Georgios Landrou, Emmanuel Stratakis,\* Georgios Charalambidis,\* Anna Mitraki,\* and Athanassios G. Coutsolelos\*

Herein, it is reported the visible-light-induced green hydrogen generation from self-assembled porphyrin-dipeptide hybrids. For the first time the self-assembly ability of a protected alanine-phenylalanine dipeptide is investigated via a simple protocol, which proved efficient in forming well-defined fibrillar architectures. These selfassembling properties are conveyed to peptide-porphyrin chromophores after their covalent conjugation. Interestingly, different architectures are observed depending on the solvent system, the solvent evaporation rate, the presence of metal in the porphyrin core, and the peripheral substitution of the porphyrin. Moving one step forward, it is explored the activity of the self-assembled nanostructures towards photocatalytic green H<sub>2</sub> production from

aqueous protons under visible-light irradiation. The distinct selfassembly behavior of the synthesized conjugates and their impact on photocatalytic hydrogen production is systematically explored in this study. Nonlinear second harmonic generation optical measurements are employed to define how the shape of the nanostructures is related to the H<sub>2</sub> production efficiency. Notably, the tubular nanostructures presented the best catalytic performance, achieving a high H<sub>2</sub> production activity of 32.7 mmol·g<sup>-1</sup>·h<sup>-1</sup>. Through detailed characterization and performance evaluation, it is aimed to uncover new insights into the design and optimization of peptide-porphyrinbased photocatalysts for sustainable energy applications.

#### 1. Introduction

The self-assembly of peptides is a widely studied phenomenon in the field of nanotechnology and materials science. [1] Peptides can form highly ordered structures through noncovalent interactions such as hydrogen bonding,  $\pi$ - $\pi$  stacking, van der Waals forces, and hydrophobic interactions. [2,3] These self-assembled structures can range from micelles, spheres, and vesicles to more complex fibrils and nanotubes, which have diverse applications in drug delivery,<sup>[4,5]</sup> tumor imaging and therapy,<sup>[2,6]</sup> tissue engineering,<sup>[7]</sup> and catalysis.<sup>[8]</sup> Dipeptides were identified as minimal self-assembling building blocks with various applications. [9] Moreover, the presence of aromatic amino acids such as phenylalanine also introduces  $\pi$ – $\pi$  interactions, contributing to the stability and morphology of the assembled structures.<sup>[10]</sup> The incorporation of protecting groups, such as the fluorenylmethoxycarbonyl (Fmoc), the tertbutoxycarbonyl (Boc) and the carbobenzoxy (Cbz) groups, can significantly influence the self-assembly behavior of dipeptides.[11,12]

Porphyrins are a class of heterocyclic macrocycle organic compounds, which play a crucial role in biological processes, such as oxygen transport, [13] as well as other applications, including photodynamic therapy, [14] artificial photosynthesis [15] and various catalytic transformations, such as hydrogen evolution reaction, [16] CO<sub>2</sub> reduction,[17] alcohol oxidation[18] and water splitting.[19] Their unique structure, characterized by a conjugated system of four pyrrole rings, conveys exceptional photophysical and photochemical

E. Triantafyllou, A. G. Coutsolelos Laboratory of Bioinorganic Chemistry Chemistry Department University of Crete 70013 Heraklion, Crete, Greece E-mail: coutsol@uoc.gr

E. Nikoloudakis, S. Psilodimitrakopoulos, D. Kavalieros, G. Landrou, E. Stratakis, A. Mitraki, A. G. Coutsolelos Institute of Electronic Structure and Laser (IESL) Foundation for Research and Technology (FORTH) 70013 Heraklion, Greece E-mail: enikoloudakis@iesl.forth.gr stratak@iesl.forth.gr

Qingdao Innovation and Development Center Harbin Engineering University Qingdao 266000, China

mitraki@materials.uoc.ar

G. Charalambidis

Theoretical and Physical Chemistry Institute (TPCI) National Hellenic Research Foundation (NHRF) 48 Vassileos Constantinou Ave., 11635 Athens, Greece E-mail: gcharal@uoc.gr

A. Mitraki

Department of Materials Science and Engineering University of Crete

Vassilika Vouton, 70013 Heraklion, Crete, Greece

Supporting information for this article is available on the WWW under https:// doi.org/10.1002/cssc.202501251

© 2025 The Author(s). ChemSusChem published by Wiley-VCH GmbH. This is an open access article under the terms of the Creative Commons Attribution-NonCommercial License, which permits use, distribution and reproduction in any medium, provided the original work is properly cited and is not used for commercial purposes.

ded from https://chemistry-europe.onlinelibrary.wiley.com/doi/10.1002/cssc.202501251 by Cochrane Greece, Wiley Online Library on [05/10/2025]. See the Terms and Conditions (https://onlinelibrary.wiley

ons) on Wiley Online Library for rules of use; OA articles are governed by the applicable Creative Commons

properties.[15] Porphyrins can absorb light across a wide range of wavelengths, making them excellent candidates for applications in photodynamic therapy, solar energy conversion, and photocatalysis.[20,21] The covalent conjugation of peptides with porphyrins combines the structural versatility of peptides with the photophysical properties of porphyrins.<sup>[22]</sup> This conjugation can lead to the formation of novel hybrid materials with enhanced or new properties.[23] In particular, the self-assembly motif of the peptide can be significantly altered upon attachment to a porphyrin moiety, resulting in distinct nanostructures. [24] These hybrid materials have the potential to improve the light-harvesting ability of porphyrins and the biocompatibility and tunability of peptides for a wide range of applications.<sup>[25]</sup> The application studied in the present study is the photocatalytic green hydrogen production.

Hydrogen is considered a clean and efficient energy carrier, and its production via photocatalysis from aqueous protons is a promising strategy for sustainable green energy generation. [26,27] The efficiency of photocatalytic systems depends on several factors, including the light absorption properties of the photocatalyst, the charge separation efficiency, and the stability of the photocatalvst. [28,29] Peptide-porphyrin conjugates offer a unique platform for designing efficient photocatalysts. [30] The peptide component can provide a scaffold that facilitates the formation of well-defined nanostructures, while the porphyrin moiety serves as the lightharvesting center.[31] More importantly, the self-assembly behavior of these conjugates can be tuned to optimize the photocatalytic activity.[32] For instance, different nanostructures such as spheres, fibrils, or vesicles can offer varied surface areas, charge separation efficiencies, and stabilities, all of which are crucial for effective photocatalysis. The development of efficient and stable photocatalysts is critical for the advancement of hydrogen production technologies.[33] By combining the unique properties of peptides and porphyrins, this study seeks to create novel hybrid materials with enhanced photocatalytic performance.[19,31] The ability to control the self-assembly of these conjugates offers a powerful tool for optimizing their functional properties.[34] Additionally, understanding the correlation of the self-assembled nanostructures with their photocatalytic activity will provide valuable insights for the design of next-generation photocatalysts.[35]

Inspired by the above, herein we studied the self-assembly ability of a previously uninvestigated dipeptide, namely Cbz-Alanine-Phenylalanine-OH (Cbz-Ala-Phe-OH). This dipeptide was selected because it combines aliphatic (Ala) with aromatic (Phe) parts, and the Cbz group attached to the N-terminus provides additional steric bulk and aromaticity.[36] Having established the ability of Cbz-Ala-Phe-OH (Scheme 1) to form fibrillar nanostructures, we examined whether this characteristic is retained after conjugation with porphyrin chromophores. We explored the self-assembling behavior of the pristine dipeptide as well as the peptide-porphyrin hybrids using a simple self-assembly protocol<sup>[30]</sup> in order to define the basic parameters that govern the morphology of the resulting architectures. Moving one step forward, we applied the various self-assembled nanostructures to a three-component photocatalytic scheme for "green" hydrogen generation from aqueous protons under visible-light irradiation. Importantly, we analyzed the impact of the distinct selfassembled morphologies on the overall photocatalytic efficiency by employing nonlinear second harmonic generation (SHG) optical measurements.

#### 2. Results and Discussion

## 2.1. Peptide Self-Assembling Investigation

We initiated our studies with the self-assembling investigation of the pristine Cbz-Ala-Phe-OH dipeptide, hereinafter referred to as ZAF (Scheme 1), which has not been reported to the literature. The interest for this dipeptide derives from its combination of aliphatic and aromatic components, while the Cbz moiety adds steric bulk and aromaticity.[36]

We first examined the architectures that this dipeptide forms in various conditions utilizing the "good-bad solvent" selfassembly protocol.[32] For the preparation of the samples, the compounds were dissolved in a chaotropic "good" solvent, and subsequently a "bad" solvent was introduced in order to induce the self-assembly process. [30] The major modulating factors that were varied during this protocol were the solvent

Scheme 1. Chemical structures of Cbz-Ala-Phe-OH, ZAF-TPP, ZAF-ZnTPP, ZAF-TMP and ZAF-ZnTMP derivatives studied in this work.

Chemistry Europe

European Chemical Societies Publishing

mixture, the ratio of the "good" and "bad" solvents, the concentration and the incubation time. The resulting morphologies were studied with scanning electron microscopy (SEM).

As illustrated in Figure 1, the dipeptide forms fibrillar microstructures when water is used as bad solvent. Occasionally, tubular structures can also be seen (Figure 1a and S1e, Supporting Information). We also examined the influence of incubation time and the concentration of the dipeptide, which were not affecting the resulting morphology (Figure S1, Supporting Information). Noteworthy, when we used other solvent combinations (Figure S2, Supporting Information) or single solvent (Figure S3, Supporting Information), malformed or amorphous architectures are observed. These observations demonstrate the significant influence of water molecules to the self-assembly of Cbz-Ala-Phe-OH dipeptide, indicating the involvement of hydrophobic interactions and hydrogen bonding during the self-assembling process. Having this knowledge in hand, we wanted to examine whether this ability is transferred to the porphyrin chromophores after the covalent connection with different porphyrins and whether the porphyrin peripheral substitution as well as the presence of metal inside the porphyrin molecule affect the selfassembly motif. Therefore, we synthesized conjugates ZAF-TPP, ZAF-ZnTPP, ZAF-TMP, and ZAF-ZnTMP (Scheme 1).

#### 2.2. Synthesis of Porphyrin-Peptide Hybrids

The porphyrin-dipeptide conjugates were synthesized via amide coupling between amino-substituted porphyrin derivatives (TPP-NH<sub>2</sub><sup>[37]</sup> and TMP-NH<sub>2</sub><sup>[38]</sup>) and commercially available dipeptide Cbz-Ala-Phe-OH as illustrated in Scheme S1, Supporting Information. Porphyrin precursor molecules TPP-NH<sub>2</sub> and TMP-NH<sub>2</sub> were coupled with Cbz-Ala-Phe-OH dipeptide using standard coupling reagents resulting in the formation of non metalated ZAF-TPP and ZAF-TMP hybrids. In the case of ZAF-TMP the presence of mesityl groups in the porphyrin periphery is expected to alter its polarity and solubility and consequently its self-assembling ability compared to the ZAF-TPP. After the amide bond formation, a straightforward metalation reaction with zinc acetate afforded the metalated ZAF-ZnTPP and ZAF-ZnTMP derivatives. The final and intermediate hybrid molecules were fully characterized by nuclear magnetic resonance (NMR), ultraviolet-visible (UV-Vis) and Fluorescence spectroscopies as well as MALDI-TOF mass spectrometry. The successful covalent attachment of porphyrin derivatives with the Cbz-Ala-Phe-OH dipeptide was verified by  $^{1}$ H and  $^{13}$ C NMR spectroscopies (Figure S4–S11, Supporting Information), where all peaks were fully assigned, as well as MALDI-TOF mass spectrometry, where we observed the corresponding molecular ions. In the  $^{1}$ H NMR spectra of both conjugates, we observed a signal that corresponds to the amide proton at  $\approx 10.4$  ppm, confirming the successful amide coupling.

## 2.3. Porphyrin-Peptide Self-Assembly

After the successful preparation of the peptide-porphyrin conjugates, we moved to their self-assembly studies via the same protocol as in the case of the Cbz-Ala-Phe-OH. Notably, we could not apply the solvents methanol (MeOH):H<sub>2</sub>O or ethanol (EtOH):H<sub>2</sub>O for comparison with the dipeptide conditions since all porphyrin hybrids were insoluble into both solvents, therefore, we examined different solvent combinations. As illustrated in Figure 2, S12, S13, Supporting Information, after the covalent attachment of the dipeptide to the nonmetalated porphyrin macrocycles, the obtained supramolecular architectures were significantly altered. Specifically, in the case of ZAF-TPP the assemblies varied from plates and fibrils to urchin- or sponge-like morphologies, while evaporation from single chaotropic solvents did not result in distinctive architectures. Contrary to ZAF-TPP, the ZAF-TMP did not show any fibrillar nanostructures. The latter hybrid self-assembled into spherical and floweror urchin-like structures (Figure 2d-f, S12, S13, Supporting Information). The above observations point out the effect of the porphyrin as well as the peripheral substitution of the macrocycle to the self-assembling properties. Since well-defined architectures were obtained also in the absence of water molecules, contrary to the case of pristine dipeptide, we can explain this result on the basis of additional Van der Waals interactions as well as  $\pi$ - $\pi$  stacking involving the porphyrin moiety. In our previous work<sup>[39]</sup> it was demonstrated that hydrogen bonding between the peptides along with  $\pi$ - $\pi$  interactions between the aromatic porphyrin macrocycles are mainly responsible for the creation of the nano-assemblies.

Having established that the solvent system, the covalent connection of chromophore, and the peripheral substitution of the porphyrin macrocycle as important factors affecting the self-assembling morphology of the peptide-based hybrids, we proceeded to invastigate the effect zinc metal cation in the porphyrin ring. **Figure 3** depicts the supramolecular assemblies obtained by

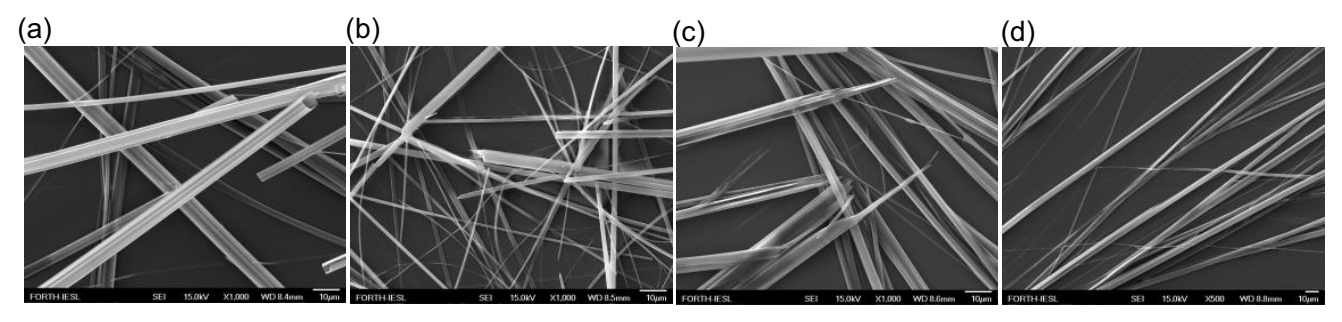


Figure 1. SEM images of Cbz-Ala-Phe-OH in a) EtOH-H<sub>2</sub>O 2:8. b) MeOH-H<sub>2</sub>O 2:8. c) THF-H<sub>2</sub>O 2:8 and d) HFIP-H<sub>2</sub>O 2:8.

onlinelibrary.wiley.com/doi/10.1002/cssc.202501251 by Cochrane Greece, Wiley Online Library on [05/10/2025]. See the Terms

on Wiley Online Library for rules of use; OA articles are governed by the applicable Creative Commons

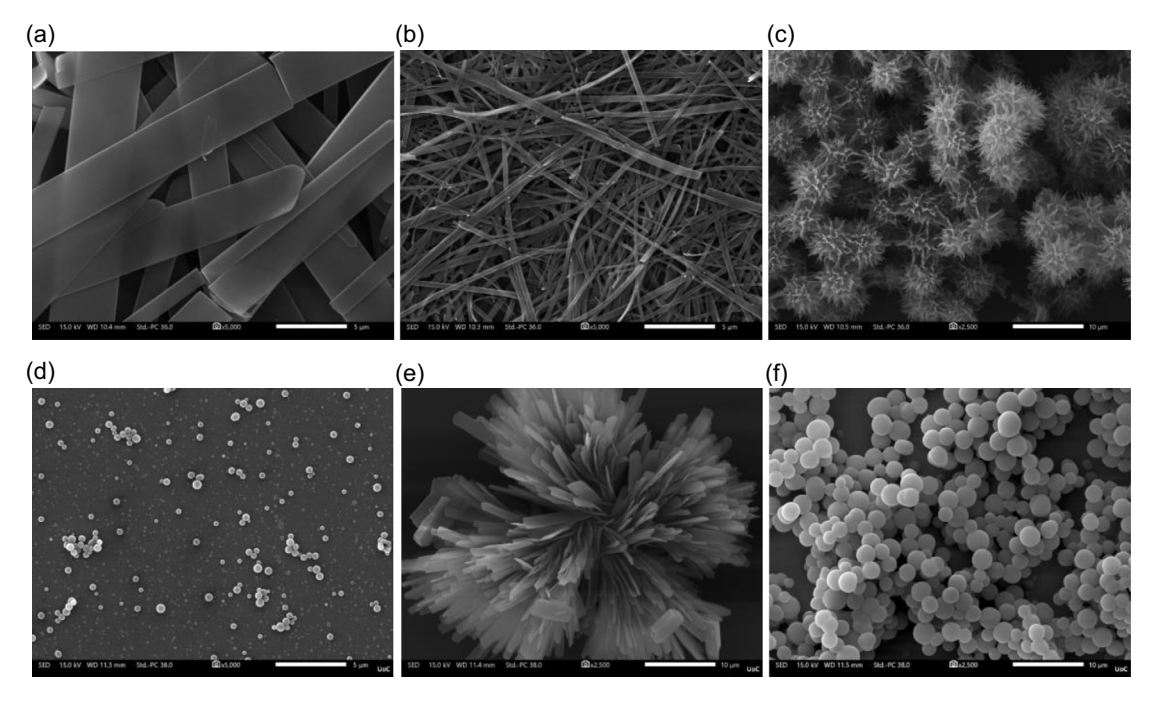


Figure 2. SEM images of ZAF-TPP in a) DCM-MeOH 2:8. b) THF-Hept. 2:8. c) HFIP-EtOH 2:8, and ZAF-TMP in d) DCM-MeOH 2:8. e) THF-Hept. 2:8. f) HFIP-EtOH 2:8. d) EtOH 2:8.

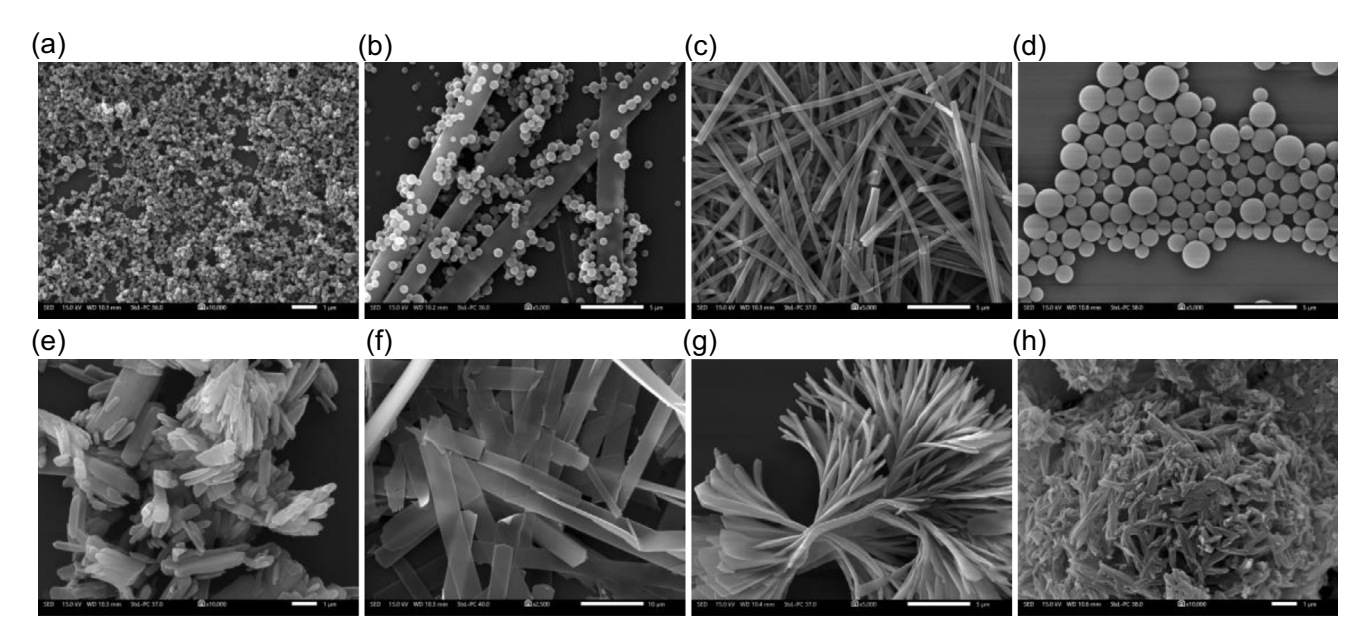


Figure 3. SEM images of ZAF-ZnTPP in a) DCM-Heptane 2:8. b) THF-MeOH 2:8. c) THF-Heptane 2:8. d) THF-H<sub>2</sub>O 2:8, and ZAF-ZnTMP in e) DCM-Heptane 2:8. f) THF-MeCN 2:8. g) THF-Heptane 2:8. h) THF- $H_2O$  2:8.

ZAF-ZnTPP and ZAF-ZnTMP in various polar and nonpolar solvent systems. ZAF-ZnTPP was able to self-assemble into nanospheres, microspheres and fibrils (Figure 3a-d, S12, S13, Supporting Information) while a mixed architecture was observed in THF-MeOH 2:8 solvent system containing fibrils decorated with uniform nanospheres (Figure 3b). The size of the spheres obtained by ZAF-ZnTPP could be easily tuned with alteration of the solvent ratio from 2:8 to 1:1 in the case of dichloromethane (DCM)-Heptane

solvent mixture (Figure S14, Supporting Information). ZAF-ZnTMP self-assembled into plates, sheets, nanospheres and microspheres while a flower-like structure was observed in THF-Heptane 2:8 mixture (Figure 3e-h, S12, Supporting Information). Noteworthy, the incorporation of the metal inside the porphyrin core resulted into different nanostructures in most solvent systems, which can be explained by the geometry change on the porphyrin moiety which becomes planar compared to the free base derivatives.

led from https://chemistry-europe.onlinelibrary.wiley.com/doi/10.1002/cssc.202501251 by Cochrane Greece, Wiley Online Library on [05/10/2025]. See the Terms and Conditions (https://onlin

ns) on Wiley Online Library for rules of use; OA articles are governed by the applicable Creative Commons

The most interesting result was obtained when we investigated the solvent evaporation rate, that is, a factor that was never examined before in these self-assembling systems. ZAF-ZnTPP self-assembled into uniform spheres with ≈1 μm radius in DCM-MeOH 2:8 solvent mixture (Figure 4a) when the solvents were rapidly evaporated using N<sub>2</sub> gas flow (evaporation within ½ minute). Interestingly, when the same solvent system was let to evaporate overnight at laboratory atmosphere, nanotubes were obtained (Figure 4b).

#### 2.4. Spectroscopic Characterization

Absorption and emission spectra analysis can provide insights into the self-assembly ability and the relative orientation of the porphyrin rings, especially by elucidating the 'H' or 'J' aggregates formation. Porphyrins display distinct sharp absorption bands in the visible region, while appropriate stacking or aggregation can broaden or shift the light absorption range. UV-Vis absorption spectra of the monomeric (in solution) and selfassembled (in solid state) ZAF-ZnTPP and ZAF-ZnTMP are presented in Figure 5. In detail ZAF-ZnTPP in DCM solution shows a strong Soret band maxima at 420 nm and two weak Q-bands at

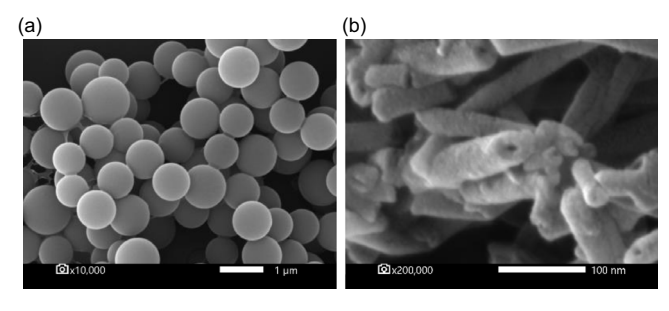


Figure 4. SEM images of ZAF-ZnTPP in DCM-MeOH 2:8 after a) fast evaporation and b) slow evaporation of the solvents.

549 (Q-1,0) and 587 nm (Q-0,0). After the self-assembly of ZAF-ZnTPP hybrids into well-defined nanostructures, the Soret band becomes broadened and redshifted. Notably, in the case of the microspheres, the Soret band is significantly more redshifted and splits into a shoulder and a prominent peak maximum at 471 nm. Similar observations were made for the ZAF-ZnTMP hybrid, although both the red-shift and broadening were less intense compared to ZAF-ZnTPP. Table S1, Supporting Information, provides the detailed list of all peak maxima for both zinc metalated derivatives. The above differences in the electronic absorption spectra of assemblies, clearly reveal the alterations in molecular stacking and aggregation, which is in agreement with the SEM observations.

Furthermore, the steady-state fluorescence emission spectra of the ZAF-ZnTPP and ZAF-ZnTMP nanostructures were measured after excitation at 420 nm (Figure 6). The molecular state of ZAF-ZnTPP in DCM solution exhibited the characteristic fluorescence signals at 599 and 645 nm, while ZAF-ZnTMP presented emission similar maxima at 597 and 646 nm. In contrast, in the self-assembled architectures, red-shifted fluorescence emission peaks were observed along with a decrease of peak intensity at ≈600 nm. These variations in the shifting of the peak and decrease of intensities are observed due to the different aggregation and stacking phenomena and are in agreement with the SEM observations.

From the above absorption and emission spectra analysis, we can conclude that the self-assemblies prepared herein consist mainly of J-aggregates (side-by-side) since red-shifted peaks were obtained in all cases.

### 2.5. SHG Measurements

In an effort to elucidate why different self-assembling motifs of the same porphyrin molecule in the same solvent conditions were obtained just by altering the solvent evaporation rate,

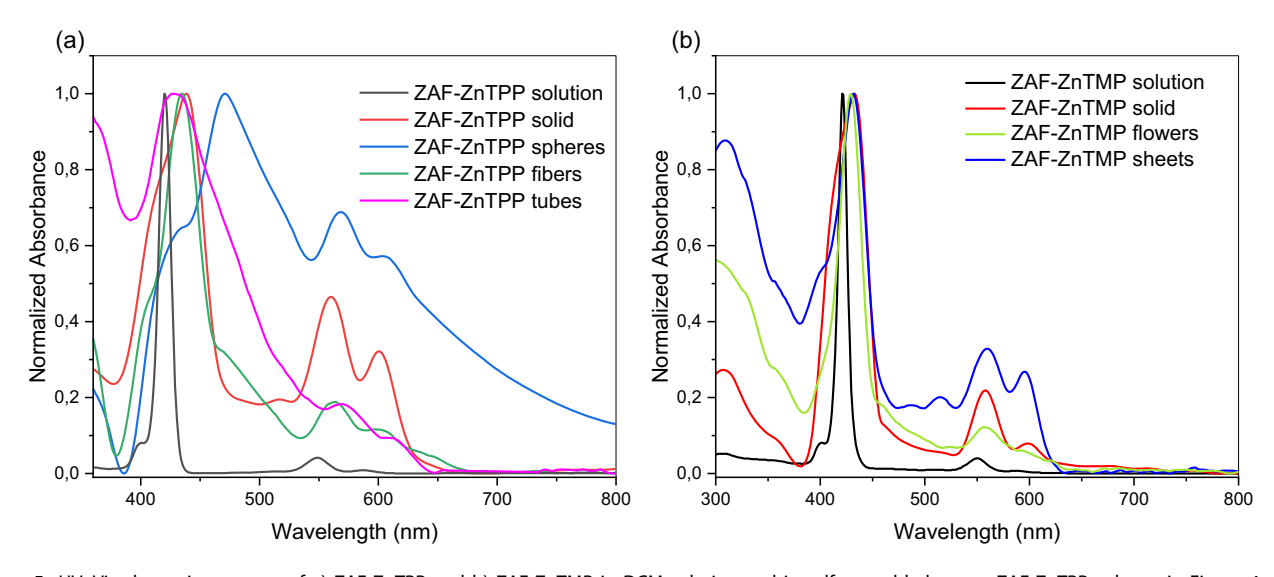


Figure 5. UV-Vis absorption spectra of a) ZAF-ZnTPP and b) ZAF-ZnTMP in DCM solution and in self-assembled states: ZAF-ZnTPP spheres in Figure 4a, ZAF-ZnTPP tubes in Figure 4b, ZAF-ZnTPP fibers in Figure 3c, ZAF-ZnTMP flowers in Figure 3g, ZAF-ZnTMP sheets in Figure 3f.

from https://chemistry-europe.onlinelibrary.wiley.com/doi/10.1002/cssc.202501251 by Cochrane Greece, Wiley Online Library on [05/10/2025]. See the Terms and Conditions (https://onlinelibrary.wiley.com/doi/10.1002/cssc.202501251 by Cochrane Greece, Wiley Online Library on [05/10/2025]. See the Terms and Conditions (https://onlinelibrary.wiley.com/doi/10.1002/cssc.202501251 by Cochrane Greece, Wiley Online Library on [05/10/2025]. See the Terms and Conditions (https://onlinelibrary.wiley.com/doi/10.1002/cssc.202501251 by Cochrane Greece, Wiley Online Library on [05/10/2025]. See the Terms and Conditions (https://onlinelibrary.wiley.com/doi/10.1002/cssc.202501251 by Cochrane Greece, Wiley Online Library on [05/10/2025]. See the Terms and Conditions (https://onlinelibrary.wiley.com/doi/10.1002/cssc.202501251 by Cochrane Greece, Wiley Online Library on [05/10/2025]. See the Terms and Conditions (https://onlinelibrary.wiley.com/doi/10.1002/cssc.202501251 by Cochrane Greece, Wiley Online Library on [05/10/2025]. See the Terms and Conditions (https://onlinelibrary.wiley.com/doi/10.1002/cssc.202501251 by Cochrane Greece, Wiley Online Library on [05/10/2025]. See the Terms and Conditions (https://onlinelibrary.wiley.com/doi/10.1002/cssc.202501251 by Cochrane Greece, Wiley Online Library on [05/10/2025]. See the Terms and Conditions (https://onlinelibrary.wiley.com/doi/10.1002/cssc.202501251 by Cochrane Greece, Wiley Online Library.wiley.com/doi/10.1002/cssc.202501251 by Cochrane Greece

ss) on Wiley Online Library for rules of use; OA articles are governed by the applicable Creative Commons Licens

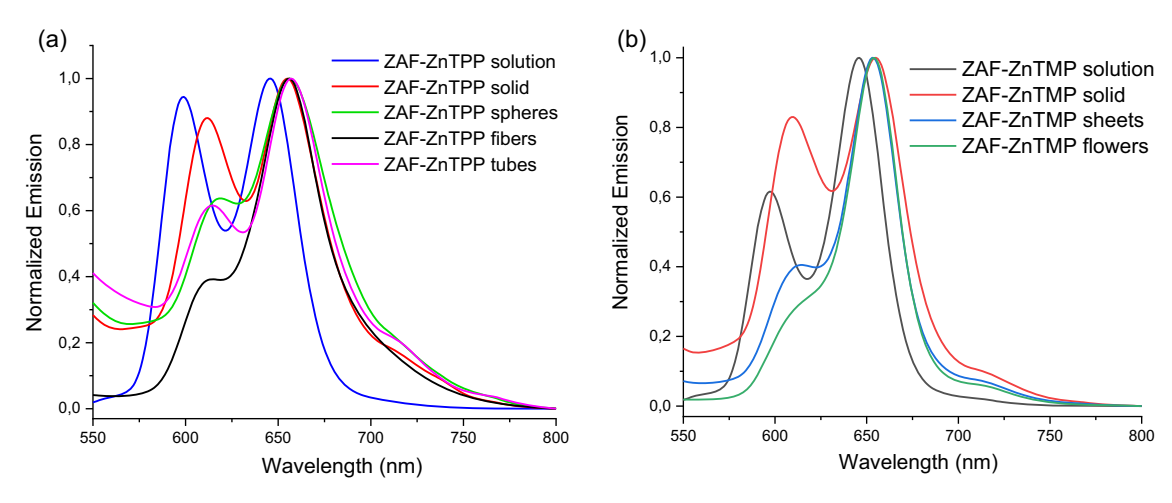


Figure 6. Fluorescence emission spectra of a) ZAF-ZnTPP and b) ZAF-ZnTMP in DCM solution and in self-assembled states: ZAF-ZnTPP spheres in Figure 4a, ZAF-ZnTPP tubes in Figure 4b, ZAF-ZnTPP fibers in Figure 3c, ZAF-ZnTMP flowers in Figure 3g, ZAF-ZnTMP sheets in Figure 3f.

we employed SHG optical measurements as a tool for evaluating the degree of porphyrin organization. In particular, we used a custom-built SHG microscope, and we performed comparative SHG intensity imaging between the different sample preparations. The SHG signals originated from the noncentrosymmetric porphyrin molecules as previously reported in the literature. [40,41] The intensity of the SHG signals in molecules is described by the following Equation [42,43]

$$I_{\mathsf{SHG}} = \chi^{(2)} \mathbf{E} \mathbf{E}$$
 (1)

where

$$\chi^{(2)} = N_{\mathsf{S}} \langle \beta \rangle \tag{2}$$

The  $\emph{E}$  is the excitation field, the  $\chi^{(2)}$  is the second-order susceptibility,  $N_{\rm S}$  is the density of molecule S and  $\langle \beta \rangle$  is the orientational average of the first hyperpolarizability. For the same molecule S (i.e., porphyrin with first hyperpolarizability  $\beta$ ) with the same molecular density  $N_{\rm S}$  in the excitation voxel, a higher SHG signal will occur due to a higher orientational average of  $\langle \beta \rangle$  that is, due to higher molecular organization.

In **Figure 7** we present SHG intensity images acquired with the same conditions (same excitation power and PMT gain) in order to compare the ZAF-ZnTPP spheres (Figure 7a) with the ZAF-ZnTPP nanotubes (Figure 7b). Both assemblies were obtained from DCM-MeOH 2:8 mixture, with the only difference being the solvent evaporation rate (Figure 4). We clearly observe higher SHG signals in Figure 7b (ZAF-ZnTPP nanotubes) than in Figure 7a (ZAF-ZnTPP spheres). This is also clearly demonstrated in Figure 7c, d where surface plots and histograms of the SHG intensity images of Figure 7a, b, are depicted, respectively. As we noted above, higher SHG signal implies higher molecular organization of the SHG-active molecules. Therefore, the ZAF-ZnTPP nanotubes (slow evaporation) present higher organization compared to ZAF-ZnTPP microspheres (fast evaporation).

## 2.6. X-Ray Diffraction Analysis of ZAF-ZnTPP Samples

XRD patterns were recorded for both the solid and self-assembled tubular forms of ZAF-ZnTPP (Figure S15, Supporting Information). The solid form exhibited a broad diffraction feature centered around  $2\theta \approx 11^\circ$ , consistent with a largely amorphous structure and lacking significant long-range order. In contrast, the self-assembled tubular ZAF-ZnTPP showed the emergence of several distinct sharp peaks at  $2\theta = 1.73^\circ$ ,  $7.25^\circ$ ,  $7.67^\circ$ , and  $31.67^\circ$ , superimposed on a similarly broad amorphous background.

The appearance of these sharp reflections upon self-assembly suggests the development of a more ordered supramolecular arrangement within the tubular structures. This increase in crystallinity likely reflects periodic packing or alignment of the porphyrin units, possibly driven by  $\pi$ - $\pi$  stacking or directional hydrogen bonding interactions. Such enhanced ordering may play a role in facilitating more efficient charge transport or light harvesting, which could correlate with the observed photocatalytic activity. [44,45]

# 2.7. X-Ray Photoelectron Spectroscopy (XPS) Analysis

To probe the surface chemical changes occurring during the photocatalytic process, XPS measurements were performed on ZAF-ZnTPP samples both in their as-prepared solid state and after photodeposition of Pt NPs. These data provide valuable insights into changes in elemental composition and oxidation states that accompany the photocatalytic transformation, which are further discussed in relation to the  $\rm H_2$  evolution results in the following section. The regions of interest include Pt 4f, Zn  $\rm 2p_{3/2}$ , N 1s, and O 1s core levels and are presented in Figure S16, Supporting Information.

No Pt 4f signal was detectable prior to reaction, indicating the absence of Pt species as expected. After photocatalysis, two well-defined peaks appear at approximately  $\approx 69.7 \, \text{eV}$  (Pt  $4f_{7/2}$ ) and  $\approx 73.0 \, \text{eV}$  (Pt  $4f_{5/2}$ ), consistent with metallic platinum (Pt°). The emergence of these peaks confirms the successful in situ

onlinelibrary.wiley.com/doi/10.1002/cssc.202501251 by Cochran

e Greece, Wiley Online Library on [05/10/2025]. See the Terms

on Wiley Online Library for rules of use; OA articles are governed by the applicable Creative Commons

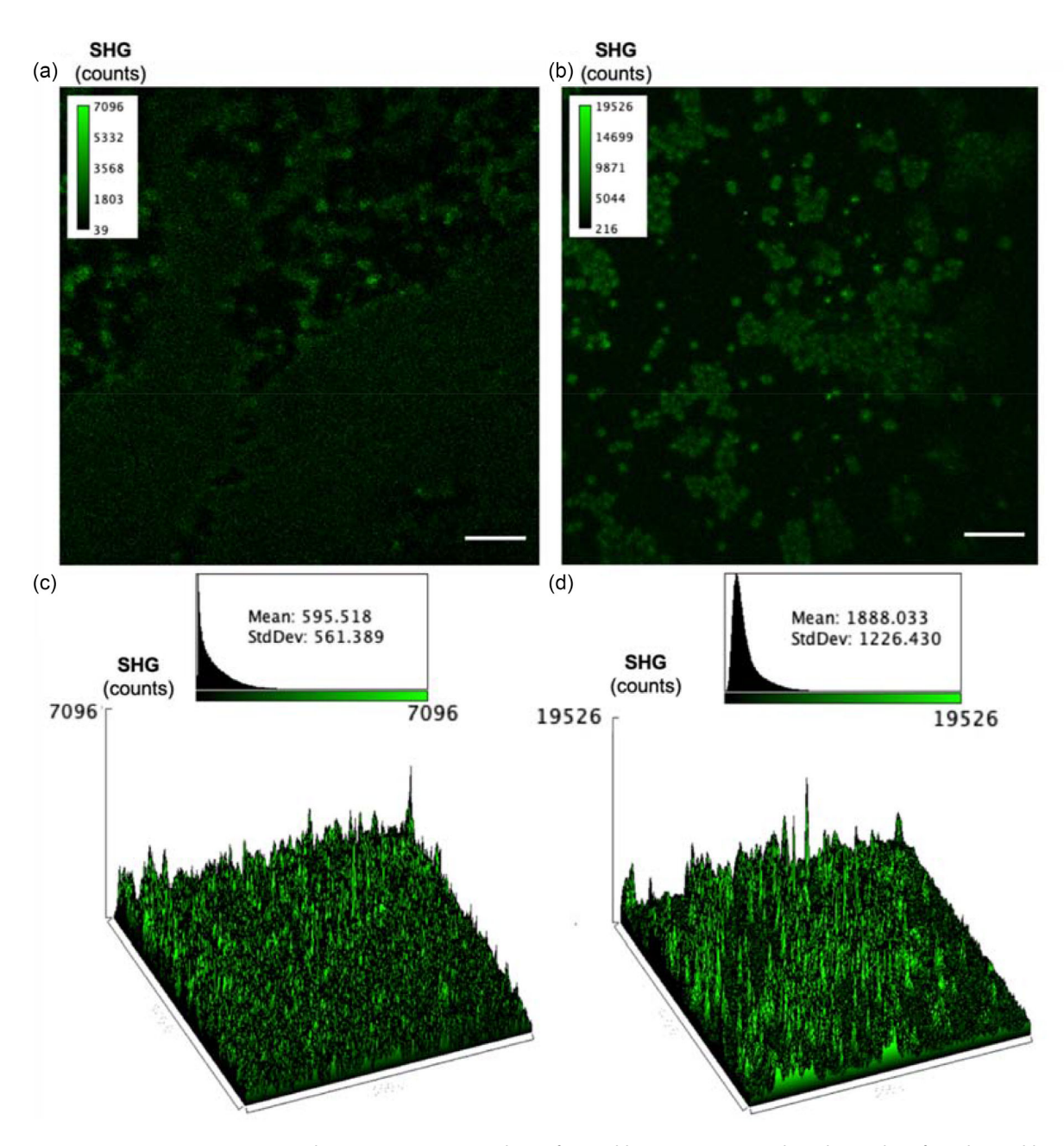


Figure 7. Comparative SHG intensity imaging between a) ZAF-ZnTPP spheres (fast) and b) ZAF-ZnTPP nanotubes (slow). c,d) Surface plots and histograms of the SHG intensity images of a,b, respectively. Scale bars show 10  $\mu$ m.

formation of Pt nanoparticles during the photocatalytic process.  $^{[46,47]}$  The Zn  $2p_{3/2}$  peak appears at  $\approx 1022$  eV in both spectra, which corresponds to  $Zn^{2+}$  coordinated within the porphyrin macrocycle.  $^{[48]}$  The lack of binding energy shift implies that the Zn center remains chemically stable during the reaction, with no detectable oxidation or reduction. Similarly, the N 1s region ( $\approx 399.5$  eV), typical of pyrrolic nitrogen coordinated to the metal center in porphyrin structures,  $^{[47]}$  and the O 1s peak at  $\approx 530$  eV show no significant shifts before and after photocatalysis, indicating that the core structure of the porphyrin is preserved. Collectively, these results confirm the successful surface formation of Pt NPs and the structural integrity of Zn-porphyrins, which support the enhanced  $H_2$  evolution activity observed.

#### 2.8. Photocatalytic Hydrogen Generation Studies

Since the target application of these conjugates was light-driven hydrogen production and zinc metalated porphyrins have been proven more efficient compared to the analogous free base molecules,  $^{[49]}$  we performed the photocatalytic investigation only for the Zn metalated derivatives. The above results showed that the optoelectronic properties of the porphyrin conjugates can be modulated by inducing different self-assembled nanostructures, so it can be presumed that the catalytic HER activity will be also modulated by the same factors since it is initiated by light absorption. Based on SEM observations we selected the most well-defined assemblies for the  $\rm H_2$  production investigation. The photocatalytic

https://chemistry-europe.onlinelibrary.wiley.com/doi/10.1002/cssc.202501251 by Cochrane Greece, Wiley Online Library on [05/10/2025]. See the Terms and Condition

on Wiley Online Library for rules of use; OA articles are governed by the applicable Creative Commons

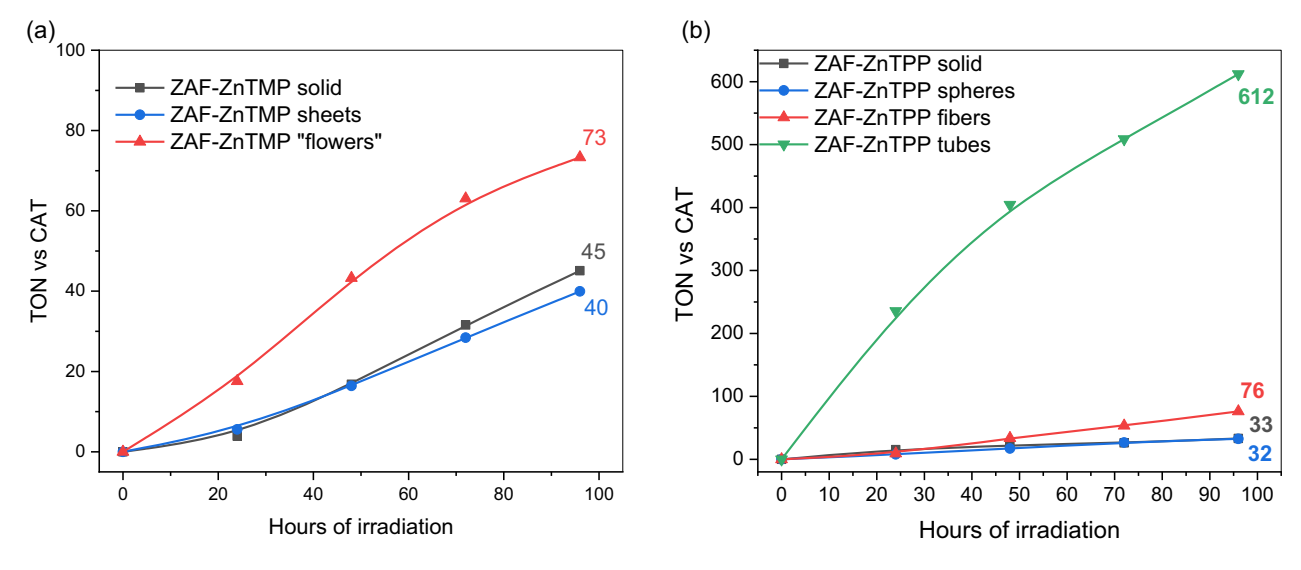


Figure 8. Photocatalytic  $H_2$  generation plots of a) ZAF-ZnTMP and b) ZAF-ZnTPP. The reported  $H_2$  production activity and the TONs are the average of three independent experiments.

experiments were performed under visible LED light irradiation using each self-assembled porphyrin hybrid as photosensitizer, an aqueous solution of ascorbic acid (AA) as sacrificial electron donor and Pt NPs as catalyst. The SED selection was based on previously reported analogous porphyrin systems which presented enhanced catalytic efficiency towards H<sub>2</sub> evolution. [32,50,51] Notably, AA has demonstrated superior performance compared to TEOA as a sacrificial electron donor in systems where the researchers compared both SED compounds.<sup>[52,53]</sup> Figure 8 illustrates the photocatalytic H<sub>2</sub> generation plots utilizing ZAF-ZnTPP and ZAF-ZnTMP self-assemblies. Significant variations in the photocatalytic activity of the systems were observed. In detail, ZAF-ZnTMP flower-like structures (obtained from THF-heptane [Hept]. 2:8 mixture; Figure 3g) reached 73 TON after 96 h of visible irradiation outperforming the corresponding amorphous solid and the nanosheets (from THF-acetonitrile [MeCN] 2:8 mixture; Figure 3f) which displayed similar performance (Figure 8a). Analogous observations were made using the ZAF-ZnTPP fibers (from THF-Hept. 2:8 mixture; Figure 3c) which presented 76 TON, two times higher activity compared to amorphous solid

and microspheres (from DCM-MeOH 2:8 mixture; Figure 4a). Noteworthy, both ZnTPP fibers and ZAF-ZnTMP flower-like structures have similar fibrillar dimensions and their enhanced activity compared to spherical nanostructure and amorphous solid is in accordance with the literature.[32] Importantly, the highest photocatalytic activity was obtained from the ZAF-ZnTPP nanotubes (obtained for the first time in the present work from DCM-MeOH 2:8 after slow evaporation of the solvents; Figure 4b) reaching 612 TON after 96 h of irradiation. The latter can be described as a  $H_2$  production rate of 32.7 mmol·g<sup>-1</sup>·h<sup>-1</sup>. To the best of our knowledge this activity is a record high performance compared to analogous systems utilizing self-assembled photosensitizer, Pt NPs as the catalysts and an aqueous solution as proton source (Table 1). This superior catalytic performance of the ZAF-ZnTPP nanotubes compared to the other nanostructures can be explained on the basis of three aspects: 1) SEM image 4b shows nanotubes with very small diameter < 100 nm resulting in much higher active surface area for catalysis to take place; and 2) SHG investigation revealed higher organization of the ZAF-ZnTPP nanotubes compared to the corresponding microspheres; 3) XRD

**Table 1.** Comparison between the best self-assembly-based photocatalytic systems for HER in the literature and this work. In all the reports below, a self-assembled photosensitizer was utilized as the PS, Pt NPs as the catalysts, and an aqueous solution as the solvent.

PS	SED	$H_2$ evolution [mmol·g <sup>-1</sup> ·h <sup>-1</sup> ]	TONs	Irr. Time [hours]	Publication
ZAF-ZnTPP	AA	32.7	612	96	This work
Fmoc-FF-ZnTPP	AA	1.96	155	406	[32]
Perylene Bisimide	MeOH	0.0127	-	3	[59]
g-C <sub>3</sub> N <sub>4</sub>	TEOA	5.8	-	2	[60]
Naphthalimide-Zn Porphyrin	TEOA	5.4	62.5	50	[61]
THPP	AA	19.5	-	5	[50]
TCPP	AA	3.5	_	6	[51]
PdTCPP-PCN-222	TEOA	3.9	_	5	[62]
Rhodamine B	AA	18.4	_	1	[63]

Chemistry Europe

European Chemical Societies Publishing

analysis revealed the appearance of sharp diffraction peaks in the nanotube sample, indicating a higher degree of structural order compared to the solid form. This increased crystallinity likely facilitates more efficient charge transport or exciton migration, further enhancing the photocatalytic activity.

Control experiments lacking the porphyrin photosensitizer, or the Pt NPs, or the SED, or light irradiation, displayed no  $\rm H_2$  production. These results point out the importance of the solvent evaporation rate to the self-assembled morphology of the photocatalysts which in turn influences the surface area and the degree of organization and eventually govern the photocatalytic activity for  $\rm H_2$  generation.

In order to determine the stability of the photocatalyst after the H<sub>2</sub> evolution experiments, UV–Vis absorption (Figure S17, Supporting Information) and MALDI-TOF (Figure S18, Supporting Information) mass spectra were recorded and confirmed that both **ZAF-ZnTPP** and **ZAF-ZnTMP** molecules remained intact after light irradiation. Therefore, the porphyrin hybrids can be efficiently recycled and used in future photocatalytic experiments, demonstrating the sustainability of our approach.

#### 3. Conclusions

In conclusion herein, we investigated the covalent conjugation of Cbz-Ala-Phe-OH peptides with porphyrins as a strategy towards the development of advanced photocatalytic materials for visible-light-induced "green" hydrogen generation. The selfassembling properties of Cbz-Ala-Phe-OH were studied for the first time via the "good-bad solvent" protocol and proved that the dipeptide self-assembles into fibrillar architectures. The covalently connected porphyrin-dipeptide hybrids formed distinct supramolecular nanostructures depending on the solvent system, the solvent evaporation rate, the presence of metal in the porphyrin core, and the peripheral substitution of the porphyrin macrocyle. Optical characterization showed the formation of J-aggregates by the nanostructures. The activity of the different self-assembled architectures towards photocatalytic green H<sub>2</sub> evolution from aqueous protons under visible-light irradiation was explored. SHG optical measurements showed that tubular nanostructures with higher molecular organization presented the highest H<sub>2</sub> generation efficiency. The enhanced H<sub>2</sub> evolution could also be attributed to their higher surface area. Noteworthy, this best-perfoming system reached a record-high H<sub>2</sub> production activity compared to analogous porphyrin based systems (Table 1). This work systematically investigated the self-assembly behavior of the synthesized conjugates and the impact of the distinct architectures on photocatalytic hydrogen production. The presence of a metal in the center of the porphyrin ring, the slow evaporation of the chosen solvent and the ability to self-assemble into tubular nanostructures were identified as critical parameters for optimal hydrogen production. Of note, the optimal building blocks were not affected during light irradiation, therefore, they could be reused for multiple experimental cycles. Beyond Pt, which was employed in this study as a standard cocatalyst, future investigations should explore the integration of earth-abundant alternatives such as Ni- and Co-based complexes, NiCu alloys, [54] Co-B nanoparticles, [55] and 2D materials like MoS<sub>2</sub>. [56] These systems have demonstrated competitive photocatalytic activity in hydrogen evolution while offering greater cost-effectiveness and scalability. Incorporating such sustainable co-catalysts into peptide–porphyrin assemblies could pave the way for the design and optimization of peptide-porphyrin-based photocatalysts towards sustainable energy applications.

# 4. Experimental Section

#### Materials

The Cbz-Ala-Phe-OH peptide was purchased from Bachem (Bubendorf, Switzerland). All reagents were purchased from common commercial sources and used without any further purification, unless otherwise stated.

#### Nuclear Magnetic Resonance (NMR) Spectroscopy

The porphyrin moieties were analyzed with <sup>1</sup>H and <sup>13</sup>C NMR spectroscopy using Bruker AMX-500 MHz and Bruker DPX-300 MHz spectrometers. All measurements were carried out at room temperature in a deuterated solvent using residual protons as internal reference.

#### **Mass Spectra**

Mass spectra were obtained on a Bruker UltrafleXtreme matrix assisted laser desorption ionization time-of-flight (MALDI-TOF) spectrometer using *trans*-2-[3-(4-tert-butylphenyl)-2-methyl-2-propenylidene] malononitrile (DCTB) as matrix.

#### **UV-Vis Absorption Spectroscopy**

In all studies, spectrometer Shimadzu UV-1700 was used. The reported solution experiments were performed using quartz cuvettes of 0.2 cm path-length. The solid-state samples were prepared via drop-casting on a quartz cover glass and left to dry overnight.

## Fluorescence Emission Spectroscopy

The emission spectra were measured on a JASCO FP-6500 fluorescence spectrophotometer equipped with a red-sensitive WRE-343 photomultiplier tube (wavelength range: 200–850 nm).

#### SEM

For SEM observations the samples were covered with 10 nm Au/Pd sputtering and were observed directly. SEM experiments were performed by using a JEOL JSM 7000 F (FESEM) operating at 15 kV.

## Synthesis: ZAF-TPP

Cbz-Alanine-Phenylalanine-OH (0.0353 gr, 0.095 mmol, 1.2 equiv.) were dissolved in a mixture of 2 mL DCM and 3 mL THF. The solution was cooled in an ice bath, N,N'-Dicyclohexylcarbodiimide (DCC,



20 mg, 0.095 mmol, 1.2 equiv.) and 1-hydroxybenzotriazole hydrate (HOBt, 13 mg, 0.095 mmol, 1.2 equiv.) were added and stirred for an extra 30 min at 0 °C. Then 1 eq of TPP-NH $_2$  (50 mg, 0.0794 mmol) was added, and the reaction mixture was let stirring at room temperature for 16 h. Washing with water (3 × 10 mL) was conducted afterwards, and the organic phase was collected, and the solvents were removed under reduced pressure. The title compound was isolated as a purple solid via column chromatography (silica gel, DCM/EtOH, 1% v/v) followed by recrystallization in DCM/Hexane mixture (41 mg, 52%). <sup>1</sup>H NMR (dimethyl sulfoxide [DMSO]-d $_6$ , 500 MHz):  $\delta$  (ppm) 10.45 (1H, s), 8.85 (2H, m), 8.28 (1H, m), 8.22 (6H, m), 8.16 (2H, d, J = 8 Hz), 8.06 (2H, d, J = 8 Hz), 7.84 (9H, m), 7.51 (1H, d, J = 7 Hz), 7.39–7.25 (10H, m), 5.06 (2H, s), 4.85 (1H, m), 4.13 (1H, m), 3.08 (1H, m), 1.23 (3H, m), -2.90 (2H, bs). MS (MALDI-TOF): m/z calculated for  $C_{64}H_{51}N_7O_{41}$ : 981.40 [M] $^+$ ; found: 981.42.

#### **ZAF-ZnTPP**

In a 50 mL flask, 20 mg of TPP-ZAF (0.020 mmol, 1 equiv.) was dissolved in 7 mL of DCM and 2 mL of CH<sub>3</sub>OH. Subsequently, Zn(CH<sub>3</sub>COO)<sub>2</sub>·2H<sub>2</sub>O (60 mg, 0.30 mmol, 15 equiv.) was added, and the reaction mixture was stirred in room temperature overnight. After the completion of the reaction, the mixture was washed with water (3  $\times$  10 mL), the organic phase was collected, and the solvents were removed under reduced pressure. The title compound was isolated by column chromatography (silica gel, DCM/EtOH, 1% v/v) as a purple solid (22 mg, 92%). <sup>1</sup>H NMR (DMSO-d<sub>6</sub>, 500 MHz):  $\delta$  (ppm) 10.41 (1H, s), 8.83 (2H, m), 8.76 (6H, m), 8.26 (1H, d, J = 8 Hz), 8.18 (6H, m), 8.12 (2H, d, J = 8.5 Hz), 8.02 (2H, d, J = 8.5 Hz), 7.78 (9H, m), 7.52 (1H, d, J = 7 Hz), 7.41-7.23 (10H, m), 5.08 (2H, s), 4.85 (1H, m), 4.14 (1H, m), 3.08 (1H, m), 1.23 (3H, m). <sup>13</sup>C NMR (DMSO-d<sub>6</sub>, 125 MHz):  $\delta$  (ppm) 172.6, 170.2, 155.8, 149.5, 149.4, 149.3, 149.2, 142.7, 138.1, 137.8, 137.6, 137.0, 134.5, 134.1, 131.6, 131.5, 129.3, 128.3, 128.1, 127.8, 127.7, 127.4, 126.6, 126.4, 120.3, 120.2, 120.1, 117.4, 65.5, 54.8, 50.3, 37.6, 18.1. MS (MALDI-TOF): m/z calculated for  $C_{64}H_{49}N_7O_4Zn$ : 1043.31 [M]<sup>+</sup>; found: 1043.30. UV–Vis (DCM)  $\lambda_{max}$ nm  $(\varepsilon/\text{mmol}^{-1}\cdot\text{dm}^3\cdot\text{cm}^{-1}) = 420 (384), 549 (15.8), 587 (3.2).$ 

#### **ZAF-TMP**

Cbz-Alanine-Phenylalanine-OH (0.0587 gr, 0.158 mmol, 1.2 equiv.) were dissolved in a mixture of 2 mL DCM and 3 mL THF. The solution was cooled in an ice bath, N,N'-Dicyclohexylcarbodiimide (DCC, 33 mg, 0.095 mmol, 1.2 equiv.) and 1-hydroxybenzotriazole hydrate (HOBt, 22 mg, 0.095 mmol, 1.2 equiv.) were added, and stirred for an extra 30 min at 0 °C. Then 1 eq of TMP-NH $_2^{38}$  (100 mg, 0.132 mmol) was added and the reaction mixture was let stirring at room temperature for 16 h. Washing with water (3 × 10 mL) was conducted afterwards and the organic phase was collected and the solvents were removed under reduced pressure. The title compound was isolated as a purple solid via column chromatography (silica gel, DCM/EtOH, 1% v/v) followed by recrystallization in DCM/Hexane mixture (120 mg, 82%). <sup>1</sup>H NMR (DMSO-d<sub>6</sub>, 500 MHz):  $\delta$  (ppm) 10.43 (1H, s), 8.82 (2H, m), 8.60 (6H, m), 8.27 (1H, d, J = 8 Hz), 8.14 (2H, d, J = 8.5 Hz), 8.04 (2H, d, J = 8.5 Hz), 7.52 (1H, d, J = 7.5 Hz), 7.37–7.25 (16H, m), 5.07 (2H, bs), 4.84 (1H, m), 4.12 (1H, m), 3.07 (1H, m), 2.58 (9H, s), 1.77 (18H, s), 1.25 (3H, m), -2.68 (2H, bs). MS (MALDI-TOF): m/z calculated for  $C_{73}H_{69}N_7O_4$ : 1107.54 [M]<sup>+</sup>; found: 1107.57.

#### ZAF-ZnTMP

In a 50 mL flask, 100 mg of TMP-ZAF (0.090 mmol, 1 equiv.) was dissolved in 35 mL of DCM and 10 mL of CH<sub>3</sub>OH. Subsequently,

Zn(CH<sub>3</sub>COO)<sub>2</sub>·2H<sub>2</sub>O (267 mg, 1.35 mmol, 15 equiv.) was added, and the reaction mixture was stirred in room temperature overnight. After the completion of the reaction, the mixture was washed with water (3  $\times$  10 mL), the organic phase was collected, and the solvents were removed under reduced pressure. The title compound was isolated by column chromatography (silica gel, DCM/EtOH, 1% v/v) as a purple solid (81 mg, 77%).  $^{1}$ H NMR (DMSO-d<sub>6</sub>, 500 MHz):  $\delta$  (ppm) 10.38 (1H, s), 8.72 (2H, m), 8.52 (6H, m), 8.25 (1H, d, J = 8 Hz), 8.09 (2H, d, J = 8.5 Hz), 7.99 (2H, d, J = 8.5 Hz), 7.52 (1H, d, J = 7 Hz), 7.40-7.25 (16H, m), 5.07 (2H, s), 4.86 (1H, m), 4.12 (1H, m), 3.27 (1H, m), 3.08 (1H, m), 2.57 (9H, bs), 1.78 (18H, bs), 1.23 (3H, m).  $^{13}$ C NMR (DMSO-d<sub>6</sub>, 125 MHz):  $\delta$  (ppm) 172.8, 170.2, 155.9, 149.2, 149.0, 148.9, 148.8, 139.2, 139.1, 135.5, 138.4, 138.1, 137.8, 137.6, 137.0, 136.8, 134.4, 131.8, 130.4, 129.9, 129.3, 128.4, 128.2, 127.8, 127.7, 127.6, 126.5, 119.2, 117.6, 117.4, 117.3, 65.5, 54.9, 50.4, 37.7, 21.7, 21.5, 21.1, 18.2. MS (MALDI-TOF): m/z calculated for  $C_{73}H_{67}N_7O_4Zn$ : 1169.45 [M]<sup>+</sup>; found: 1169.44. UV–Vis (DCM)  $\lambda_{max}$ nm ( $\varepsilon$ /mmol<sup>-1</sup>·dm<sup>3</sup>·cm<sup>-1</sup>) = 421 (410), 550 (16.6), 588 (2.8).

#### **Preparation of Self-Assembled Samples**

For the preparation of the samples, the corresponding compounds were dissolved in a chaotropic solvent (DCM, THF, 1,1,1,3,3,3-hexafluoroisopropanol [HFIP]), and subsequently a "bad" solvent (MeOH, EtOH,  $H_2O$ , MeCN, Heptane) was introduced. After 24 h of incubation, 10  $\mu L$  of each sample were placed on a 12 mm cover glass and left to dry overnight before observation via SEM.

#### SHG Imaging Microscope

The SHG optical measurements were performed using the experimental setup illustrated in Figure S19, Supporting Information, and described earlier.<sup>[57]</sup> Briefly, the fundamental beam originates from a fs oscillator (FLINT, Light Conversion) centered at 1030 nm, with 80 MHz repetition rate, and 50 fs pulse duration (according to the manufacturer). Then, the beam was directed to a pair of galvanometric mirrors (GM) (6215 H, Cambridge Technology), which provide the raster-scanning scheme needed for imaging. Then the beam was entering into a modified microscope (Axio Observer Z1, Zeiss), is reflected by a mirror (PFR10-P01, ThorLabs) placed at the turret box of the microscope and reaches the objective lens (Plan-Apochromat 40x/1.3NA, Zeiss). At the sample plane (SP), the SHG signals (generated at 515 nm) were collected in the forward direction using a high-numerical-aperture condenser lens (C) (achromatic-aplanatic, 1.4NA, Zeiss). The signals were then filtered through a short-pass filter (SPF) (FF01-680/SP, Semrock) and a band-pass filter (BPF) (FF01-514/3, Semrock) before detected by a photomultiplier tube (PMT) (H9305-04, Hamamatsu). The SPF blocks the laser light from reaching the detector, while the BPF allows only the SHG at 515 nm to be detected.

# **Photocatalytic Measurements**

The photocatalytic  $H_2$  production experiments were conducted in glass vials (10.2 mL) sealed with a rubber septum, at ambient temperature and pressure. Before each experiment, a fresh buffer solution was prepared. More precisely, the buffer solution was a 1M aqueous solution of ascorbic acid (AA) that was adjusted to pH=4 using an aqueous solution of NaOH (5M). For each photocatalytic experiment, 4 mg of porphyrin compound were added in the glass with 5 mL of the buffer solution and 0.2 mg  $Na_2PtCl_6\cdot 6H_2O$  (5% w/w). For the preparation of the self-assembled samples, we followed the self-assembled protocol inside the glass vials and let the solvents evaporate overnight (only in the case of fast evaporation sample we used

from https://chemistry-europe.onlinelibrary.wiley.com/doi/10.1002/cssc.202501251 by Cochrane Greece, Wiley Online Library on [05/10/2025]. See the Terms and Conditions (https://onlinelibrary.wiley.

on Wiley Online Library for rules of use; OA articles are governed by the applicable Creative Commons License

 $N_2$  flow). The samples were sonicated for 30 s. In order to achieve anaerobic conditions, the suspensions were degassed using nitrogen for 5 min (in an ice/water bath). Finally, the samples were sealed with a silicon septum and were irradiated under continuous stirring with a low-power white LED lamp ring with color temperature 6400 K and lumen of 3800 LM. This set-up provided defined positions and certain amount (50 W·cm $^{-2}$ ) of the emitted light for all the vials simultaneously. The amount of  $H_2$  production of each sample vial was determined using a Shimadzu GC 2010 plus chromatograph with a TCD detector and a molecular sieve 5 Å column (30 m - 0.53 mm). For every measurement, 100  $\mu$ L were taken from the headspace of the

Calculation of TONs and  $H_2$  evolution mmol( $H_2$ )·g(cat)<sup>-1</sup>·h<sup>-1</sup>

are the average of three independent experiments.

The catalytic performance values were calculated according to the equations

vial and were instantly injected in the GC. In all cases, both the

reported H<sub>2</sub> production values and the turn over number (TON)

$$TON = \frac{n(H_2)}{n(Cat)}$$
 (3)

$$H_2$$
 evolution rate (mmol  $g^{-1}h^{-1}$ ) =  $\frac{n(H_2)}{m(catalyt) \times t}$  (4)

where:  $n(H_2)$  is the total amount of the produced  $H_2$  (in mmol) and n(Cat) is the total amount of the Pt catalyst (in mmol).

In every photocatalytic experiment  $0.0002\,g$  of  $Na_2PtCl_6.6H_2O$  were used. Thus, the final amount of the catalyst (Pt) in each experiment is m (catalyst) =  $0.000069\,g$ .

An apparent quantum yield (AQY) of roughly 0.28% was obtained. The energy of photons was determined by using a StarLite power meter with a FL400A-BB-50 thermal sensor (Ophir Optronics Ltd). The apparent quantum efficiency (AQY) was calculated according to the following Equation<sup>[58]</sup>

$$AQY = \frac{33.2296 \times \mu mol \, of \, H_2 \times number \, of \, e^- \, for \, H^+ \, to \, H_2}{light \, intensity \, \times \, area \, \times \, time \, \times \, wavelength} \tag{5}$$

where: light intensity in mW/cm<sup>2</sup>, area: irradiation area in cm<sup>2</sup>, time in hours, and wavelength: irradiation wavelength in nm ( $533 \pm 10$  nm).

# **Acknowledgements**

The European Commission's Horizon Europe Research Programme under Grant Agreement Number 101120397 (project no: APPROACH) and the Special Research Account of the University of Crete are gratefully acknowledged for the financial support. Emmanouil Nikoloudakis gratefully acknowledges the Bodossaki Foundation for financial support.

#### Conflict of Interest

The authors declare no conflict of interest.

# Data Availability Statement

The data that support the findings of this study are available from the corresponding author upon reasonable request. **Keywords:** hydrogen evolution reaction  $\cdot$  hydrogen production  $\cdot$  peptides  $\cdot$  photocatalysis  $\cdot$  porphyrins  $\cdot$  self-assembly

- [1] T. Li, X.-M. Lu, M.-R. Zhang, K. Hu, Z. Li, Bioact. Mater. 2022, 11, 268.
- [2] B. Sun, K. Tao, Y. Jia, X. Yan, Q. Zou, E. Gazit, J. Li, Chem. Soc. Rev. 2019, 48, 4387.
- [3] C. J. C. Edwards-Gayle, I. W. Hamley, Org. Biomol. Chem., 2017, 15, 5867.
- [4] Z. Fan, L. Sun, Y. Huang, Y. Wang, M. Zhang, Nat. Nanotechnol. 2016, 11, 388.
- [5] S. Yang, M. Wang, T. Wang, M. Sun, H. Huang, X. Shi, S. Duan, Y. Wu, J. Zhu, F. Liu, Mater. Today Bio 2023, 20, 100644.
- [6] Y. Deng, W. Zhan, G. Liang, Adv. Healthc. Mater., 2021, 10, 2001211.
- [7] J. Chen, X. Zou, Bioact. Mater. 2019, 4, 120.
- [8] Q. Liu, A. Kuzuya, Z.-G. Wang, iScience 2023, 26, 105831.
- [9] L. Adler-Abramovich, E. Gazit, Chem. Soc. Rev. 2014, 43, 6881.
- [10] M. Reches, E. Gazit, Phys. Biol. 2006, 3, S10.
- [11] A. Levin, T. A. Hakala, L. Schnaider, G. J. L. Bernardes, E. Gazit, T. P. J. Knowles, *Nat. Rev. Chem.* 2020, 4, 615.
- [12] I. W. Hamley, ACS Appl. Bio Mater. 2023, 6, 384.
- [13] M. Tahoun, C. T. Gee, V. E. McCoy, P. M. Sander, C. E. Müller, RSC Adv. 2021, 11, 7552.
- [14] J. Han, Y. Liu, D. Peng, J. Liu, D. Wu, Bioconjug. Chem. 2023, 34, 2155.
- [15] R. Das, P. Kumar Verma, C. M. Nagaraja, Coord. Chem. Rev. 2024, 514, 215944.
- [16] W. Zhang, W. Lai, R. Cao, Chem. Rev. 2017, 117, 3717.
- [17] B. Mondal, P. Sen, A. Rana, D. Saha, P. Das, A. Dey, ACS Catal. 2019, 9, 3895.
- [18] G. Di Carlo, C. Albanese, A. Molinari, S. Carli, R. Argazzi, A. Minguzzi, F. Tessore, E. Marchini, S. Caramori, ACS Appl. Mater. Interfaces 2024, 16, 14864.
- [19] D. D. La, H. H. Ngo, D. D. Nguyen, N. T. Tran, H. T. Vo, X. H. Nguyen, S. W. Chang, W. J. Chung, M. D.-B. Nguyen, *Coord. Chem. Rev.* 2022, 463, 214543.
- [20] O. H. Olubowale, Q. Do, N. K. Arachchige, D. G. Hebert, J. C. Garno, ACS Appl. Nano Mater. 2024, 7, 12214.
- [21] A. Charisiadis, E. Glymenaki, A. Planchat, S. Margiola, A.-C. Lavergne-Bril, E. Nikoloudakis, V. Nikolaou, G. Charalambidis, A. G. Coutsolelos, F. Odobel, *Dyes Pigm.* 2021, 185, 108908.
- [22] A. Llamosí, M. P. Szymański, A. Szumna, Chem. Soc. Rev 2024, 53, 4434.
- [23] H. Wei, J. Min, Y. Wang, Y. Shen, Y. Du, R. Su, W. Qi, J. Mater. Chem. B 2022, 10, 9334.
- [24] P. Pathak, M. A. Zarandi, X. Zhou, J. Jayawickramarajah, Front. Chem. 2021, 9, 764137.
- [25] R. Chang, E. Nikoloudakis, Q. Zou, A. Mitraki, A. G. Coutsolelos, X. Yan, ACS Appl. Bio Mater. 2020, 3, 2.
- [26] L. Li, J. Yan, T. Wang, Z.-J. Zhao, J. Zhang, J. Gong, N. Guan, Nat. Commun. 2015. 6, 5881.
- [27] H. Ishaq, I. Dincer, C. Crawford, Int. J. Hydrogen Energy 2022, 47, 26238.
- [28] J. S. O'Neill, L. Kearney, M. P. Brandon, M. T. Pryce, Coord. Chem. Rev. 2022, 467, 214599.
- [29] V. Nikolaou, E. Agapaki, E. Nikoloudakis, K. Achilleos, K. Ladomenou, G. Charalambidis, E. Triantafyllou, A. G. Coutsolelos, *Chem. Commun.* 2023, 59, 11256.
- [30] E. Nikoloudakis, M. Pigiaki, M. N. Polychronaki, A. Margaritopoulou, G. Charalambidis, E. Serpetzoglou, A. Mitraki, P. A. Loukakos, A. G. Coutsolelos, ACS Sustain. Chem. Eng. 2021, 9, 7781.
- [31] Y. Fu, L. Zhang, X. Yan, K. Liu, ChemSystemsChem, 2024, 7, e202400068.
- [32] V. Nikolaou, G. Charalambidis, A. G. Coutsolelos, Chem. Commun. 2021, 57, 4055.
- [33] C.-C. Chan, C.-C. Chang, C.-H. Hsu, Y.-C. Weng, K.-Y. Chen, H.-H. Lin, W.-C. Huang, S.-F. Cheng, Int. J. Hydrogen Energy 2014, 39, 1630.
- [34] W. J. Mullin, S. A. Sharber, S. W. Thomas III, J. Polym. Sci. 2021, 59, 1643.
- [35] A. Chakravorty, S. Roy, Sustainable Chem. Environ. 2024, 8, 100155.
- [36] A. Wu, H. Yamamoto, Chem. Sci. 2023, 14, 5051.
- [37] E. Nikoloudakis, K. Karikis, J. Han, C. Kokotidou, A. Charisiadis, F. Folias, A. M. Douvas, A. Mitraki, G. Charalambidis, X. Yan, A. G. Coutsolelos, *Nanoscale* 2019, 11, 3557.
- [38] K. Y. Chiu, Y. O. Su, Chem. Commun. 2009, 2884, https://doi.org/10.1039/ B903374M.
- [39] G. Charalambidis, E. Georgilis, M. K. Panda, C. E. Anson, A. K. Powell, S. Doyle, D. Moss, T. Jochum, P. N. Horton, S. J. Coles, M. Linares,



- D. Beljonne, J.-V. Naubron, J. Conradt, H. Kalt, A. Mitraki, A. G. Coutsolelos, T. S. Balaban, *Nat. Commun.* **2016**, *7*, 12657.
- [40] F. Tessore, G. Di Carlo, A. Forni, S. Righetto, F. Limosani, A. Orbelli Biroli, Ingranics 2020, 8, 45.
- [41] M. O. Senge, M. Fazekas, E. G. A. Notaras, W. J. Blau, M. Zawadzka, O. B. Locos, E. M. Ni Mhuircheartaigh, Adv. Mater. 2007, 19, 2737.
- [42] P. J. Campagnola, L. M. Loew, Nat. Biotechnol. 2003, 21, 1356.
- [43] P. J. Campagnola, C.-Y. Dong, Laser Photonics Rev. 2011, 5, 13.
- [44] Y. Guo, Q. Zhou, B. Zhu, C. Y. Tang, Y. Zhu, EES Catal. 2023, 1, 333.
- [45] S. Wang, F. He, Y. Lu, Y. Wu, Y. Zhang, P. Dong, X. Liu, C. Zhao, S. Wang, D. Wang, J. Zhang, S. Wang, J. Colloid Interface Sci. 2024, 654, 317.
- [46] D. Zang, Z. Huo, S. Yang, Q. Li, G. Dai, M. Zeng, L. Ruhlmann, Y. Wei, Mater. Today Commun. 2022, 31, 103811.
- [47] A. Modak, P. Bhanja, A. Bhaumik, ChemCatChem 2019, 11, 1977.
- [48] S. Tehrani Nejad, R. Rahimi, M. Rabbani, S. Rostamnia, Sci. Rep. 2022, 12, 17121.
- [49] P. Zhang, M. Wang, C. Li, X. Li, J. Dong, L. Sun, Chem. Commun. 2010, 46. 8806.
- [50] N. Zhang, L. Wang, H. Wang, R. Cao, J. Wang, F. Bai, H. Fan, Nano Lett. 2018, 18, 560.
- [51] J. Jing, J. Yang, Z. Zhang, Y. Zhu, Adv. Energy Mater. 2021, 11, 2101392.
- [52] R. Chen, Y. Wang, Y. Ma, A. Mal, X.-Y. Gao, L. Gao, L. Qiao, X.-B. Li, L.-Z. Wu, C. Wang, Nat. Commun. 2021, 12, 1354.
- [53] L. Zani, M. Melchionna, T. Montini, P. Fornasiero, J. Phys. Energy 2021, 3, 031001.
- [54] D. Spanu, S. Recchia, S. Mohajernia, O. Tomanec, Š. Kment, R. Zboril, P. Schmuki, M. Altomare, ACS Catal. 2018, 8, 5298.

- [55] S. Gupta, C. Prapaitrakool, B. R. Bhagat, C.-L. Yeh, A. Dashora, A. Sirisuk, N. Patel, N. Daneu, A. Kocjan, M. Spreitzer, J. C. S. Wu, M. M. Kržmanc, Int. J. Hydrogen Energy 2024, 60, 1288.
- [56] K. Ahmad, T. H. Oh, Catalysts 2025, 15, 648.
- [57] G. M. Maragkakis, S. Psilodimitrakopoulos, L. Mouchliadis, A. S. Sarkar, A. Lemonis, G. Kioseoglou, E. Stratakis, Adv. Opt. Mater. 2024, 12, 2401321.
- [58] S. Fang, M. Rahaman, J. Bharti, E. Reisner, M. Robert, G. A. Ozin, Y. H. Hu, Nat. Rev. Methods Primers 2023, 3, 61.
- [59] D. McDowall, B. J. Greeves, R. Clowes, K. McAulay, A. M. Fuentes-Caparrós, L. Thomson, N. Khunti, N. Cowieson, M. C. Nolan, M. Wallace, A. I. Cooper, E. R. Draper, A. J. Cowan, D. J. Adams, *Adv. Energy Mater.* 2020, 10, 2002469.
- [60] J. Zhang, Y. Huang, T. Nie, R. Wang, B. He, B. Han, H. Wang, Y. Tian, Y. Gong, Appl. Surf. Sci. 2020, 499, 143942.
- [61] G. B. Bodedla, J. Huang, W.-Y. Wong, X. Zhu, ACS Appl. Nano Mater. 2020, 3, 7040.
- [62] L. Xiao, Q. Zhang, X. Wang, H. Shuai, H. Lu, X. Li, X. Yang, H. Zhang, Appl. Surf. Sci. 2024, 655, 159590.
- [63] S. H. Bu, W. Cho, G. Ham, B. Yang, J. Jung, H. Cha, C. Park, Angew. Chem., Int. Ed., 2025, 64, e202416114.

Manuscript received: July 3, 2025 Revised manuscript received: August 28, 2025 Version of record online: